Journal of Nondestructive Evaluation (2018) 37:8
https://doi.org/10.1007/s10921-018-0462-8

Broadband Calibration of Acoustic Emission and Ultrasonic Sensors from Generalized Ray Theory and Finite Element Models

Bill S. Wu[1] · **Gregory C. McLaskey**[1]

Received: 29 August 2017 / Accepted: 9 January 2018
© Springer Science+Business Media, LLC, part of Springer Nature 2018

Abstract
This paper describes a calibration method for acoustic emission and ultrasonic sensors that is effective from 1 kHz to 1 MHz. The method combines generalized ray theory and finite element analysis to model wave propagation at higher and lower frequencies, respectively. A ball impact is used as a calibration source, a thick aluminum plate is used as the test block, and hot glue is used as the couplant. We demonstrate this method on five commercial piezoelectric sensors: Physical Acoustics (PAC) R15a, PAC WSa, Panametrics V101, Panametrics V103, and Valpey-Fisher Pinducer. Our calibration results show that reflections and other wave phases can be more clearly identified with the less-resonant Panametrics sensors. The PAC sensors have the greatest sensitivity and are able to detect surface normal displacements at least down to 1 pm amplitude in the 100s of kHz frequency band. Aperture effect is minimized by the small size of the Pinducer. Our method focuses on the amplitude response of the sensors (phase is ignored) and extends the calibration to a frequency band that is lower than typical analyses. Low frequency information is useful for determining the seismic moment of a seismic source (analogous to the magnitude of an earthquake) and can increase the amount of information acquired in a single recording.

Keywords Broadband sensor calibration · Generalized ray theory · Finite element · Aperture effect · Couplant · Absolute sensitivity

1 Introduction

Acoustic emission (AE) and ultrasonic sensors can detect transient sources of kHz- to MHz-frequency vibrations that arise from source mechanisms ranging from tensile cracking (e.g. [1]) to shear slip events (e.g. [2,3]) to granular flow (e.g. [4]). Quantitative characterization (i.e. calibration) of such sensors, allows researchers to link recorded signals to physically meaningful quantities and separate the source mechanisms and wave propagation effects from the distortions or resonance introduced by the sensor and recording system. Calibration also allows the relative merits of different sensor models to be compared. Purely electrostatic or electromagnetic transducers that are reversible (can be used as a source and receiver of mechanical energy) have been calibrated using reciprocity techniques (e.g. [5–7]), but this approach cannot be used for sensors with built-in preamplifiers. We report on a calibration approach that lumps the sensor response, the effects of coupling, and any preamplification into a single instrument response function. This technique utilizes a comparison of the recorded signal, $s(\boldsymbol{x}, t)$ to the mechanical disturbance felt by the sensor that produced the signal. In this paper, we assume the mechanical disturbance to be displacement time history $u(\boldsymbol{x}, t)$, but similar methods can utilize velocity or another physical quantity (acceleration, strain, etc.).

Past researchers have determined $u(\boldsymbol{x}, t)$ either by direct measurement with a reference sensor or from theory wherein the elastodynamic solution is determined from numerical simulation by finite element (FE) analysis or a generalized ray theory approach. While making direct measurements of $u(\boldsymbol{x}, t)$ using a laser interferometer [8] or another reference sensor [9], both the reference transducer and the sensor under testing are placed in locations symmetric about the source. If the source is repeatable, they can also be placed in the same location. In practice, reference transducers need to be high fidelity, high sensitivity, absolutely calibrated, and are often expensive. In this work, we describe calibration techniques that utilize $u(\boldsymbol{x}, t)$ estimated from theory. We use both FE analysis [10–12], and generalized ray theory [13–16] to

✉ Gregory C. McLaskey
gcm8@cornell.edu

[1] Cornell University, 220 Hollister Dr., Ithaca, NY 14850, USA

Published online: 18 January 2018

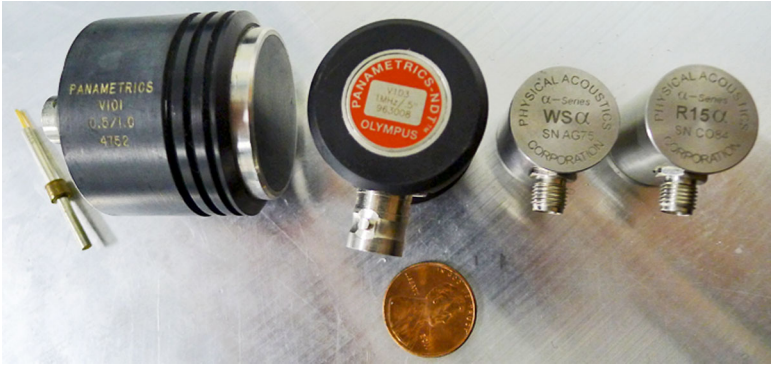

Fig. 1 Photograph of the five commercial sensors. From left to right: Valpey-Fisher Pinducer, Panametrics V101, Panametrics V103, PAC WSa, PAC R15a. A U.S. penny is shown for reference

estimate the surface displacement time history to which a recorded signal is compared.

Calibration results are expressed as the instrument response function in the time domain as $i(t)$, or the instrument response spectrum in the frequency domain as $I(\omega)$, which is determined over a specific frequency band. Here we refer to $I(\omega)$ simply as the "calibration curve". Since the instrument response obtained in this procedure contains information about the entire measurement system including sensor, coupling, cables, and digitizer, we try to calibrate the sensors under conditions similar to those used in typical experiments.

In this paper, we describe techniques to increase the bandwidth over which the calibration is valid to span three decades, from 1 kHz to 1 MHz. Previous calibration procedures have traditionally focused on 100 kHz to 1 MHz (e.g. [6,9,16]) and neglected lower frequencies where sensor sensitivity diminishes. Spectral amplitude at low frequencies is related to the seismic moment, or magnitude, of discrete sources of seismic waves, and recent work has shown that AE sources range from magnitude -6 down to -10 [1–3]. Our extension of the calibration to lower frequencies can aid in the estimation of the seismic moment as well as radiated energy and the corner frequency, which is related to the spatial and temporal dimensions of the source (e.g. [2]). Lower frequency information can also be important for other wideband analysis methods including diffuse wavefield techniques developed in the past 15 years (e.g. [17,18]).

A complete characterization of instrument effects includes both the amplitude and phase of $I(\omega)$. Here, we focus on the determination of the amplitude, which is all that is needed for many signal analysis techniques described above. To simulate or remove the distorting effects of the sensor in the time domain, both amplitude and phase information are needed, and techniques of this type are described in [16] for the 100 kHz to 1 MHz frequency band.

At low frequencies (<50 kHz), details of sensor behavior are often unclear due to inherent uncertainty of spectral estimates made using recordings with short time windows [19]. To extend the calibration curve to lower frequencies, we obtain long-time-duration calculations of the mechanical disturbance using FE models.

At high frequencies, the calibration is limited by attenuation and scattering, which cause the signal-to-noise ratio (SNR) to drop significantly. If not explicitly accounted for, these effects can cause an apparent loss of sensitivity at high frequencies. Another influencing factor for sensor calibration experiments at high frequency is the aperture effect. When the direction of wave propagation is parallel to the sensor surface, multiple wavelengths will average over the finite sensor contact area and decrease the recorded wave amplitude, as described in Sect. 3.4.

In Sect. 2, we describe the transfer function framework upon which our calibration approach relies. We also describe the modeling of elastic wave propagation using both generalized ray theory and FE models. In Sect. 3 we describe how the instrument response $I(\omega)$ is obtained from recorded signals and $u(\boldsymbol{x}, t)$, and we concatenate the calibration curves derived from the different methods to form a broadband calibration curve. Figure 1 shows a photograph of the five types of commercial sensors used to demonstrate the broadband calibration technique. Their properties are listed in Table 1 and differences in their instrument responses are discussed in Sect. 3. In Sect. 4, we demonstrate how the hot glue used as a couplant causes frequency-dependent attenuation of the recorded signal.

2 Methods

2.1 Calibration Framework

The sensor characterization experiments cast wave propagation and instrumentation effects into a transfer function framework, as defined by previous work [8,16,20–22]. This framework assumes that wave propagation and sensor response can be modeled as linear, time-invariant systems. Wave propagation between the source and sensor is mathematically described as convolution with the Green's function, $G_{kj}(\boldsymbol{x}, t; \boldsymbol{\xi}, \tau)$, which denotes the displacement at x at time

Table 1 Commercial sensors used in calibration experiments

Name	Manufacturer	Diameter (mm)	Published resonance frequency (MHz)
V103	Panametrics	12.7	1
V101	Panametrics	25.4	0.5
WSa	Physical Acoustics	19.1	0.1–1
R15a	Physical Acoustics	19.1	0.15
Pinducer	Valpey-Fisher	2.3	Unspecified

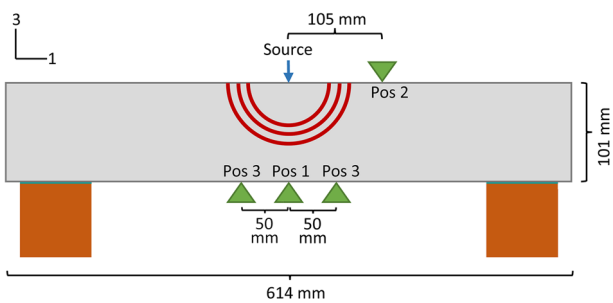

Fig. 2 Schematic diagram of the test specimen. Its length in the out-of-plane dimension is 614 mm. The test specimen rests on a pair of 90 × 90 mm wooden blocks topped with a 1.6 mm thick layer of cork. The source location is shown by an arrow and sensor positions for the different calibration tests are shown as triangles

t in the k-direction due to an impulse loading at $\boldsymbol{\xi}$ at time τ in the j-direction. We obtain the Green's function solutions using generalized ray theory [23,24] or FE analysis (Sect. 2.4). Similarly, the instrumentation effect (a combined effect including the digitizer, cables, sensor, and couplant) are mathematically described as convolution with the instrument response, $i(t)$:

$$s(\boldsymbol{x}, t) = f_j(\boldsymbol{\xi}, \tau) * G_{kj}(\boldsymbol{x}, t; \boldsymbol{\xi}, \tau) * i_k(t), \tag{1}$$

where $s(\boldsymbol{x}, t)$ is the recorded signal from a sensor at location x at time t, $f_j(\boldsymbol{\xi}, \tau)$ is a force–time function that describes the source at location $\boldsymbol{\xi}$ at time τ in the j-direction (Sect. 2.3). Summation convention is implied. '*' denotes convolution in the time domain.

The calibration source described in this work acts normal to the surface of the test specimen (the 3 direction, Fig. 2). The sensors under calibration are primarily sensitive to the 3 direction ($i(t) \cong i_3(t)$). In this case, Eq. 1 can be further simplified:

$$s(\boldsymbol{x}, t) = u_3(\boldsymbol{x}, t) * i_3(t), \tag{2}$$

where the displacement is defined as $u_3(\boldsymbol{x}, t) = f_3(\boldsymbol{\xi}, \tau) * G_{33}(\boldsymbol{x}, t; \boldsymbol{\xi}, \tau)$.

To compute the instrument response, $i(t)$, we wish to deconvolve the theoretical displacement from the recorded signal. Deconvolution becomes division in the frequency domain, so it is more convenient to compute the instrument response spectrum:

$$I(\omega) = \frac{S(\boldsymbol{x}, \omega)}{U(\boldsymbol{x}, \omega)} = \frac{S(\boldsymbol{x}, \omega)}{F(\boldsymbol{\xi}, \omega) G(\boldsymbol{x}, \omega; \boldsymbol{\xi}, \omega)} \tag{3}$$

where $S(\boldsymbol{x}, \omega)$, $U(\boldsymbol{x}, \omega)$, $F(\boldsymbol{\xi}, \omega)$, and $G(\boldsymbol{x}, \omega; \boldsymbol{\xi}, \omega)$ are the Fourier transforms of $s(\boldsymbol{x}, t)$, $u(\boldsymbol{x}, t)$, $f(\boldsymbol{\xi}, t)$, and $G(\boldsymbol{x}, t; \boldsymbol{\xi}, \tau)$, respectively.

When working in the frequency domain, individual samples of the discrete Fourier transform (DFT) are inherently uncertain, so we take the average of many samples of the DFT that fall into the same frequency bin. We desire frequency bins that are equally spaced on a log scale, but the samples of the DFT (the Fourier frequencies) are linearly spaced every $\mathrm{d}f$, (where $\mathrm{d}f = 1/T$ and T is the length of the time window). As a result, the lowest frequency bins contain only a few samples of the DFT. We chose a frequency resolution of 17 frequency bins per decade and required at least $\mathrm{n}_{\min} = 3$ samples of the DFT in each frequency bin. This results in the relationship $\frac{1}{17} = log_{10}\left(\frac{f_{\min} + n_{\min}\mathrm{d}f}{f_{\min}}\right)$. Solving for $f_{\min}$, we find the minimum reliable frequency based on our time window T and averaging scheme

$$f_{\min} \approx 20\,\mathrm{d}f = 20/T. \tag{4}$$

2.2 Test Setup

Calibration experiments were performed on a rectangular aluminum plate resting on 90 mm by 90 mm wooden blocks topped with a 1.6 mm thick layer of cork. The dimensions of the plate are 614 mm by 614 mm by 100 mm in the 1, 2, and 3 directions. The propagation speed of longitudinal and shear waves in the aluminum are measured to be 6.3 and 3.0 km/s, respectively. Figure 2 shows a schematic diagram of the test setup. The source is a ball dropped 900 mm onto the top center of the plate. When testing in sensor position 1, (epicenter location) directly beneath the source, the main waveform feature is the longitudinal (P) wave and reflections through the thickness of the plate occurring at equal time increments (P, PPP, 5P, etc). Theoretically, we expect no vertical displacement from S waves due to its radi-

ation pattern [10], but we can still identify a near-field term that produces a discontinuity in the vertical displacement at the time of the S wave arrival. Aperture effect is minimized at position 1 because most wave arrivals (besides the later-arriving reflections off the side of the test specimen) are normal to the sensor face (incidence angle = 90°). At sensor position 2, the direction of propagation is parallel to the plate surface (incidence angle = 0°). The aperture effect will be most severe (shown in Sect. 3.4). The main waveform feature is the Rayleigh surface wave that travels slower than the S wave. Sensors were coupled to the plate using hot glue, and the effects of this coupling are compared to a Vaseline couplant using two identical sensors at position 3, as described in Sect. 4.1.

2.3 Calibration Source

Many sources have been used in calibration experiments, including the glass capillary fracture [9], pencil lead break [25], laser-generated pulse [26,27], and ball impact [16,28]. Ball impact is selected as the source in this paper because its frequency content can be controlled by selection of ball size, it has a force–time function that is readily derived from Hertzian theory and can be easily applied to a FE model, it can be treated as a point source (source area $\ll 1$ mm), it acts only in the surface-normal direction, and it is inexpensive and convenient.

For the ball impact, a spherical ball is dropped vertically onto the test plate inside a transparent cylindrical tube (0.9 m tall, 60 mm in diameter). By Hertz impact theory, the precise forcing function is formulated from the stress equilibrium equation and the force deformation relation [28,29]:

$$f(t) = f_{\max} \sin\left(\frac{\pi t}{t_c}\right)^{1.5}, \quad 0 \le t \le t_c, \tag{5}$$

where $f_{\max} = 1.92\rho^{0.6}(\delta_1+\delta_2)^{-0.4} R_1^2 v_0^{1.2}$ is the maximum force upon impact and $t_c = 4.53\left(\frac{4\rho_1\pi(\delta_1+\delta_2)}{3}\right)^{0.4} R_1 v_0^{-0.2}$ is the contact time. In preceding equations, $\delta_i = \left(1-\mu_i^2\right)/(\pi E_i)$, and E and μ are the Young's modulus and Poisson's ratio, respectively. R_1 and v_0 are the radius and incoming velocity of the ball. Subscript 1 refers to the material of the ball and subscript 2 is the material of the more massive test specimen. Equation 4 was verified experimentally for a variety of materials [28] and for balls of different diameters dropped at different heights (Sect. 3.2).

Table 2 lists the properties of the balls used in the calibration experiments. Figure 3 shows the theoretical force–time functions determined from Eq. 5 and their respective spectra for selected sources. From Fig. 3b we observe that the spectra all have flat amplitude at low frequencies with amplitude equal to the ball's change in momentum ΔP. Above the corner frequency $f_0 = 1/t_c$ spectral amplitudes decrease and are characterized by a series of lobes separated by zeros. The zeros makes solving for the sensor instrument response challenging. Thus, we assume each source is only valid up to f_0. Small balls have the higher f_0 and are used to extend the high frequency range of the calibration. Larger balls generate better SNR at low frequencies.

The ball's change in momentum ΔP can be determined from Hertzian theory as $\Delta P = \int f(t)\,dt = v_0 - v_{\text{rebound}}$ where $f(t)$ is found from Eq. 5. This formulation assumes

Table 2 Properties of 0.9 m high ball drops used in calibration experiments

Ball diameter (mm)	Material	Corner frequency f_0 (kHz)	Change in momentum ΔP (N s)
0.5	Ruby	1200	3.7e−7
0.8	Titanium	640	0.9e−5
2.38	Steel	150	3.0e−4
3.15	Steel	140	0.7e−3
4.75	Steel	77	2.4e−3

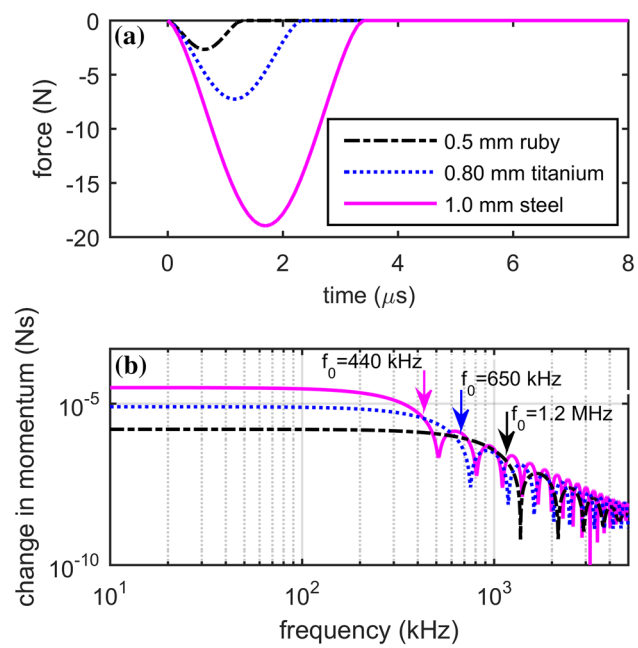

Fig. 3 Force–time functions and their spectra. **a** Force–time function of three different ball impact sources derived theoretically from Hertzian theory (Eq. 5) assuming a drop height of 1 m onto aluminum. Balls with smaller diameter generally have a smaller contact time t_c and amplitude. **b** Frequency spectra of the same sources. Notice the spectrums share a general pattern: flat at low frequencies followed by a series of lobes at high frequencies above the corner frequency $f_0 = 1/t_c$. The amplitude at low frequencies is equal to the change in momentum of the ball upon impact with the test block

that no energy is lost in the elastic impact ($v_0 = -v_{\text{rebound}}$). In reality, the local contact stresses often exceed the yield stress of the aluminum, and tiny dents are visible in the test plate. Yet, energy dissipation due to plastic yielding and other deviations from purely elastic, Hertzian contact primarily affect frequencies higher than f_0 [28]. Below f_0, where we utilize the ball source, spectra depend only on the ball's change in momentum, which can be measured from the ball's drop height h_1 and rebound height h_2, and used to make a small correction. In our experiments, the steel balls dropped from $h_1 = 0.91$ m onto the aluminum test plate rebounded to $h_2 = 0.21$ m. Since $v_o = \sqrt{2gh}$, the change in momentum of the ball $\Delta P \propto \left(\sqrt{h_1} + \sqrt{h_2}\right)$ which is only 74% of the change in momentum assumed by Hertz theory. Thus a $20 * \log_{10}(0.74) = -2.6$ dB correction was made.

2.4 Wave Propagation: Determination of Green's Function

Analytical solutions for the wave equation have been derived for an infinite half space [30]—the elastodynamics of stresses and strain in an elastic body are governed by Navier's equation, which can be derived by substituting the kinematic and constitutive relations of an isotropic material into the equation of motion. For our sensor calibration experiments, we find the solution to the wave equation in the form of a Green's function $G(\boldsymbol{x}, t; \boldsymbol{\xi})$, described in Sect. 2.1. We obtain the Green's function using two techniques. The first is a generalized ray theory solution for an infinite plate [24]. The second utilizes FE analysis.

2.4.1 Generalized Ray Theory

Pao et al. [23] first calculated the Green's function for an isotropic elastic plate in the form of an infinite series expansion, in which each term represents a ray path. Explicit formulae for Green's function solutions have been developed for the infinite plate in Fortran [24] and translated to MATLAB [28]. The accuracy of the solutions has been verified against theory [30] by McLaskey and Glaser [28]. By assuming an infinite plate, generalized ray theory is only valid before reflections off the sides of the test plate arrive at the sensor location. This limits the time duration (T) that can be studied using this Green's function approach, which creates a lower limit for the calibration bandwidth: $f_{\text{min}} = 50$ kHz for $T = 400\,\mu$s, based on Eq. 4.

2.4.2 Finite Element

We use FE analysis as a second method of calculating the Green's function. Previously, the FE method has been used to model elastic waves in an elastic solid [10–12,31]. We use the FE method to extend the theoretical displacement time history $u(\boldsymbol{x}, t)$ to significantly longer durations so that the sensor instrument response at lower frequencies can be estimated. The FE model can take into account the reflections from the sides of the plate which are not accounted for by the generalized ray theory code. Although a 2D axial-symmetric FE model can act as a starting point for understanding wave propagation inside the plate, we used a 3D model that is capable of generating more accurate reflections from the plate's sides.

Explicit analysis was used instead of implicit analysis since it is more computationally efficient. Explicit analysis does not enforce equilibrium of internal structure forces with externally applied loads, thereby eliminating the need to reconstruct the global stiffness matrix at every time step. The stability of the FE solution is influenced by the element size (a) of the model with respect to the minimum wavelength of elastic waves that a selected source introduces into the plate. As a rule of thumb, we allocate five elements to span the minimum wavelength of interest (λ_m), which can be estimated using the shear wave velocity (C_S) and the corner frequency (f_0) of the source:

$$a = \frac{1}{5}\lambda_m = \frac{1}{5}\frac{C_S}{f_0}, \tag{6}$$

ANSYS Explicit Dynamics was used to perform all the FE simulations in this study. The geometry of the 3D model matched that of the actual test specimen. No boundary conditions were applied, so the plate was effectively floating in space. We justify this in Appendix A by experimentally showing that, when the plate is resting on wooden blocks, boundary conditions do not significantly affect the first 50 ms of vibrations felt at the center of the aluminum plate down to 1 kHz. We input the force time history of the ball (Sect. 2.3) as a point force into the model, and obtained the displacement time history at the epicenter location. The material constants were computed from the longitudinal and shear wave speeds, C_p and C_S measured in the plate material [32]:

$$\mu = \frac{\alpha^2 - 2}{2\left(\alpha^2 - 1\right)}, \quad E = C_P^2 \rho \frac{(1+\mu)(1-2\mu)}{1-\mu}, \tag{7}$$

where E, μ and ρ are the elastic modulus, Poisson's ratio, and density of the test specimen and $\alpha = C_p/C_s$.

The FE Green's function can be computed in the frequency domain:

$$G_{\text{FE}}(\omega) = \frac{U(\omega)}{F(\omega)}, \tag{8}$$

Where $U(\omega)$ is the Fourier transform of the displacement time history obtained from the FE model, and $F(\omega)$ is the FT of the force–time function applied to the FE model. Note that the FE solution is not accurate at high frequencies or when

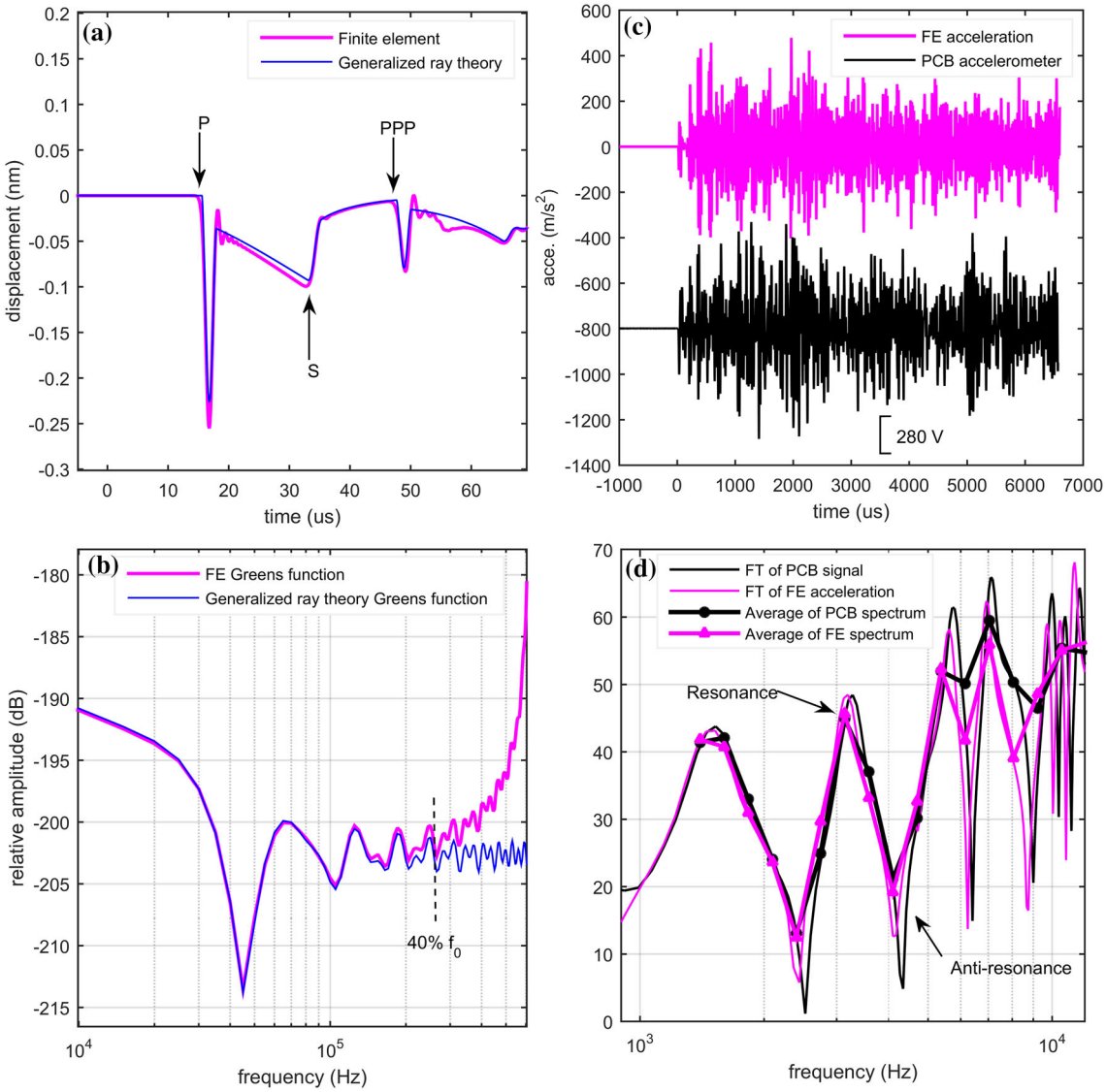

Fig. 4 Validation of the FE model using the force–time functions of the 0.8 mm titanium ball (**a**, **b**) and 3.15 mm steel ball (**c**, **d**) as input. In **a**, **c** the impact of the ball onto the plate occurs at t = 0. **b** Fourier transform of the Green's function computed from FE and generalized ray theory (**d**) Fourier transform of the PCB accelerometer recorded signal and FE acceleration are shown alongside averaged spectra resampled with 17 frequency bins per decade, as described in Sect. 2.1

$F(\omega) = 0$. $G_{\mathrm{FE}}(\omega)$ is only valid at frequencies above 20 df (Eq. 4) and below $0.4 f_0$, as described in the next section.

2.4.3 Validation of Finite Element Model

Figure 4 shows the validation of FE simulations against generalized ray theory at short times/high frequencies and against a PCB accelerometer (model 352C03) at longer times/lower frequencies. At short time duration, before side reflections arrive at the epicenter location, the FE-derived Green's function was computed (Eq. 8) and compared with generalized ray theory to validate its high frequency component (Fig. 4a, b). The force–time function of a 0.8 mm Titanium ball was chosen as an input to the FE model. A fine mesh (0.9 mm element size) was necessary to capture the high frequency energy content of the source ($f_0 = 640$ kHz, Table 2), making the FE model costly to run (large file size, RAM requirements, etc.). There is excellent agreement in the time domain (Fig. 4a). The only discrepancy occurs around 18 µs in the form of spurious oscillations due to the zero-energy modes of the FEs [10]. These are excited because some energy is input into the model at frequencies higher than its f_0. At high frequencies, the FE-derived Green's function starts to diverge from the generalized ray theory Green's function (Fig. 4b), but is accurate to within 2 dB for frequencies up to $0.4 f_0$.

Next, the validation was extended to lower frequencies using a long duration FE-generated time series. The force–time history of a 3.15 mm steel ball was chosen because it has a low corner frequency (140 kHz, Table 2). With increased source diameter, the FE model can be meshed using coarser elements, significantly reducing computation cost. Even larger ball sizes were not chosen because different wave arrivals (P, S, PPP, etc.) would be indiscernible due to the long contact time (Sect. 2.3).

For validation of the FE model at low frequencies, we cannot compute the Green's function via generalized ray theory because it doesn't account for the side reflections and becomes computationally expensive due to the many rays required. Instead, we differentiated the FE displacement time history twice to produce an acceleration time history, and compared this to the recorded signal from a PCB accelerometer (Fig. 4c, d). At the lower frequencies (1–10 kHz) the spectra are dominated by the plate's resonances and anti-resonances, as shown in Figs. 4d and 5e. As a result, small differences (in C_p, C_s, dimensions, etc.) between the FE model and the true test block, which cause a slight mismatch in the locations of resonant peaks and result in significant differences in spectral amplitudes. This can limit the accuracy of the calibration in this low frequency band, but after averaging the samples of the DFT into logarithmically-spaced frequency bins, as described in Sect. 2.1, the spectra of the FE solution the accelerometer signal agree to within a few dB, with somewhat larger differences (10 dB) in the 6–8 kHz band.

3 Results

3.1 General Procedure for Broadband Calibration

In this section we describe a procedure to obtain a broadband calibration, spanning three decades in frequency from 1 kHz to 1 MHz. Once we have established a well-defined source (Sect. 2.3) and verified the Green's function by FE analysis and generalized ray theory (Sect. 2.4.3), we can calculate the instrument response using an input/output pair of theoretical displacement ($u(\boldsymbol{x}, t)$) and recorded signal ($s(\boldsymbol{x}, t)$). We determine $u(\boldsymbol{x}, t)$ using generalized ray theory for a short time window to determine $I(\omega)$ for high frequencies, and we determine $u(\boldsymbol{x}, t)$ using the FE model for a longer time window to determine $I(\omega)$ for lower frequencies. We then concatenate the two segments of $I(\omega)$ together to create a broadband calibration curve. We first demonstrate the technique with the V103 sensor and compare this sensor's instrument response to the others in Sect. 3.3.

The upper limit of the calibration is determined by the upper frequency band of the source (Fig. 3). The source with the highest f_0 (0.5 mm ruby ball, Table 2) was chosen. To capture energy up to f_0, a FE model would need 0.5 mm elements (Eq. 6, Sect. 2.4.2) and would be costly to run. Thus, we used generalized ray theory to compute $u(\boldsymbol{x}, t)$ for the ruby ball source and compared it to the recorded signal in the time domain (Fig. 5a). Once $u(\boldsymbol{x}, t)$ and $s(\boldsymbol{x}, t)$ were obtained, they were Fourier transformed in an identical fashion, and spectral ratios were taken (Eq. 3, Fig. 5b, c). We show the amplitude of $I(\omega)$ and ignore phase information in this study. Both signals were sampled at 10 MHz, windowed with a 400 µs Blackman–Harris window centered on the first wave arrival. Fourier transforms were performed with the fast Fourier transform (FFT) algorithm.

As mentioned in Sect. 2.1, the lower limit of the calibration is determined by the time duration (T) of the time series and the manner in which the spectrum is averaged. Following Eq. 5, the lower bound of the sensor instrument response is $20/\mathrm{T} = 50$ kHz (Fig. 5c). A longer time window T can extend the lower bound of the sensor calibration. The FE model is the best candidate to extend $u(\boldsymbol{x}, t)$. The ideal source for the FE model should have a low f_c so that coarser elements are adequate to capture its energy content. At the same time, its corner frequency should be greater than 50 kHz to ensure there is overlap between the two segments of $I(\omega)$. Based on the corner frequencies of the different sources (Table 2), a 3.15 mm diameter steel ball was chosen for low frequency calibration. A FE simulation using 5 mm elements (Eq. 6) was computed to T = 11 ms (Fig. 5d).

The instrument response $I(\omega)$ from generalized ray theory (Fig. 5c) and FE (Fig. 5e) are shown with reference lines corresponding to displacement, velocity, and acceleration. Phase information is not shown. From 100 kHz to 1 MHz, the V103 has a nearly linear response and measures a physical quantity between velocity and displacement. There is a distinctive decrease in sensitivity at 20 kHz as shown in Fig. 5f. In the 1–10 kHz frequency band, the sensor sensitivity decreases and the slope of the frequency response nearly matches that of acceleration; thus the V103 can be considered an accelerometer in this frequency band. Figure 5e shows the resonances and anti-resonances of the test plate that are apparent at lower frequencies (1–10 kHz). The S-wave wavelengths (0.3–3 m) in that frequency range are within an order of magnitude of the plate's length (0.6 m). We observe a similar trough between 40 and 50 kHz in Fig. 5b that is due to reflections traversing the thickness of the plate. These peaks and troughs in $G(\omega)$ make the computation of $I(\omega)$ sensitive to wave velocities and geometry assumed in the FE and generalized ray theory models and decreases the accuracy of the calibration in this 1–10 kHz frequency band. Consequently, we perform the spectral averaging technique described in Sect. 2.1 before computing the spectral ratios in order to help retain accuracy at the expense of frequency resolution.

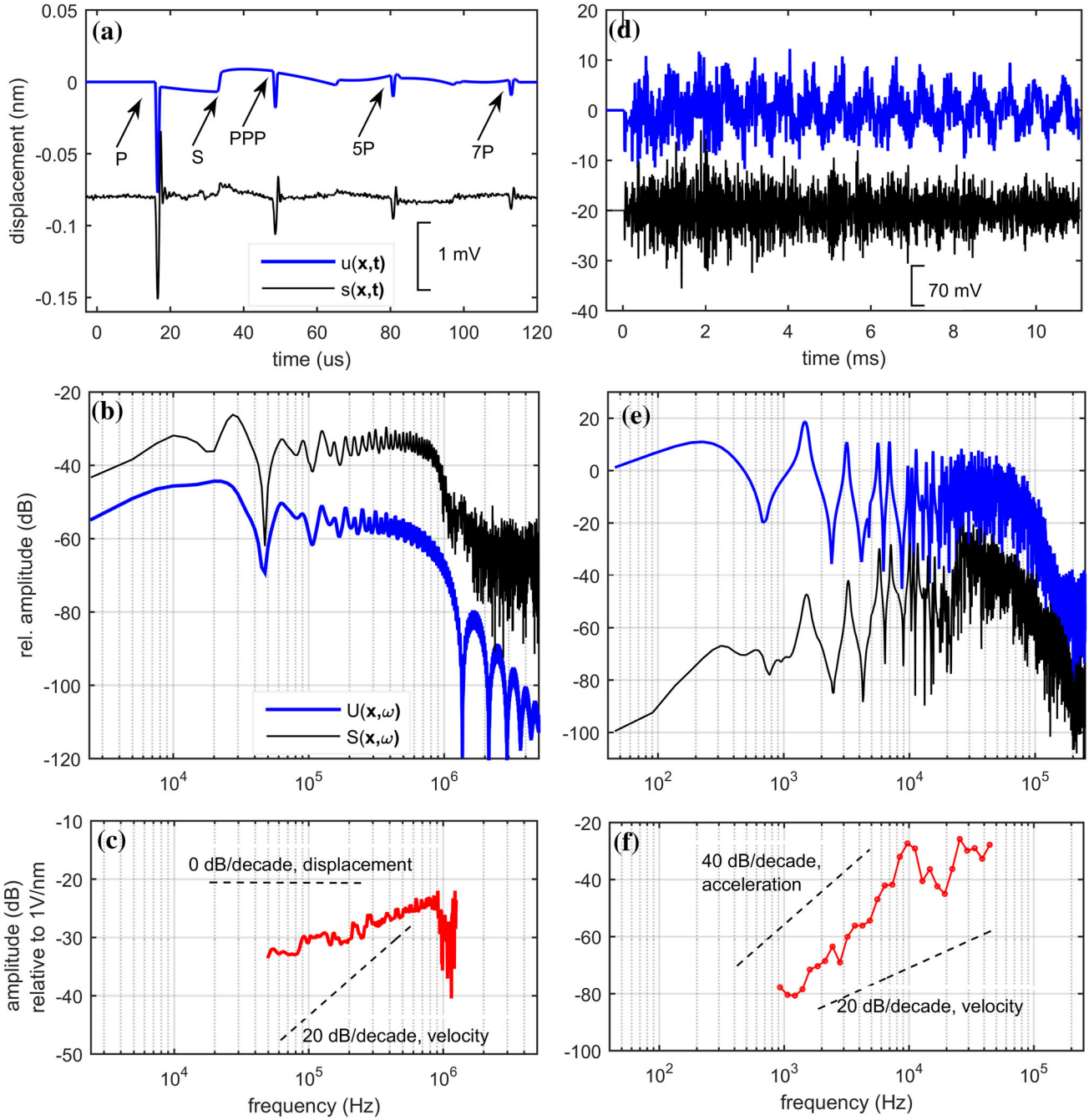

Fig. 5 Calibration results for Panametrics V103 (**a**). Theoretical displacement $u(\boldsymbol{x}, t)$ and recorded signal $s(\boldsymbol{x}, t)$ at epicenter location of a 0.5 mm ruby ball impact. The impact of the ball onto the plate is at t = 0. The recorded signal is normalized to the first P-wave arrival (40 mV/nm), and then offset vertically [identical treatment is performed in (**d**)]. The first P-/S- arrivals are labeled. **b** Fourier transforms of the signals in (**a**) are offset vertically for better comparison. The troughs near 40 kHz correspond to an anti-resonance of the test plate. **c** $I(\omega)$ is computed by spectral division (Eq. 3) using $U(\boldsymbol{x}, \omega)$ and $S(\boldsymbol{x}, \omega)$. **d** Recorded signal $s(\boldsymbol{x}, t)$ and FE simulated theoretical displacement $u(\boldsymbol{x}, t)$ of a 3.15 mm diameter steel ball for 11 ms. **e** Fourier transforms of the signals in (**d**) are shifted vertically for better comparison. **f** $I(\omega)$ is computed by spectral division (Eq. 3) using $U(\boldsymbol{x}, \omega)$ and $S(\boldsymbol{x}, \omega)$ that were resampled with 17 frequency bins per decade

3.2 Validity of Source Model

Before implementing the broadband calibration technique on other commercial sensors, the validity of the source model (Eq. 5) was tested using sources of various diameters (D) from different drop heights (h). For each case (D, h), the spectral ratio of $S(\omega)/F(\omega)$ should be identical (Eq. 3). Figure 6 shows $S(\omega)/F(\omega)$ calculated using signal processing techniques described in Sect. 3.1 and plotted to each source's corner frequency. A variety of D, h yields $S(\omega)/F(\omega)$ that

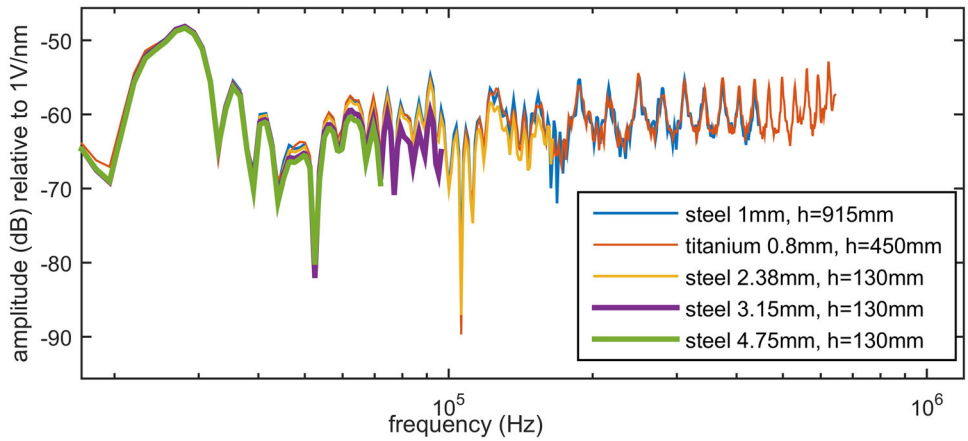

Fig. 6 Validation of the source model using different diameter sources dropped from multiple heights. Each curve is $S(\omega)/F(\omega)$ and is plotted up to the corner frequency of its corresponding source

agree to within 3 dB up to 640 kHz, effectively validating the shape of the Hertzian source model proposed in Sect. 2.3.

3.3 Broadband Calibration Curves

Figure 7 compares the responses of five commercial sensors (PAC R15a, PAC WSa, V103, V101, pinducer) in time and frequency domains. Figure 7a shows the theoretical displacement time history $u(\boldsymbol{x}, t)$ from generalized ray theory and the output from the five commercial sensors at the epicenter location (position 1 in Fig. 2) using the 0.5 mm ruby ball as a source. Hot glue was the couplant between the sensor and the aluminum test plate and the responses shown include attenuation due to the hot glue (described in more detail in Sect. 4.1.1). Figure 7b contains the concatenated instrument response for each commercial sensor that contains a high frequency segment derived using generalized ray theory and a low frequency segment derived from FE analysis.

Observations about the commercial sensors are made based on Fig. 7. Time domain oscillations can be associated with frequency domain resonances. The PAC R15a time series contains many oscillations (ringing) following the initial P arrival with a period of approximately 7 µs, which corresponds to the distinctive resonant peak at 150 kHz visible in $I(\omega)$. (This matches the manufacturer-specified resonance.) Later arrivals (S, 3P, etc) are buried in the resonant "coda". The PAC WSa also contains some ringing after the initial P-wave arrival but has less dominant resonances, and a correspondingly smoother instrument response from 100 kHz to 1 MHz. As a result, later P-wave reflections can be discerned. Peak sensitivity is at about 550 kHz. Both Panametrics sensors, V103 and V101, clearly show the initial P-wave arrival and its reflections through the thickness of the plate (3P, 5P, etc) as well as the initial S-wave arrival, shown as an upward discontinuity between the P and 3P. Peak sensitivities of the V101 and V103 are around 500 kHz and 1 MHz, consistent with published resonant frequencies. The Pinducer has "coda" oscillations and many large resonances of $I(\omega)$ at high frequency. The PAC sensors, while more resonant than the Panametrics sensors, are 20–40 dB more sensitive from 50 kHz to 1 MHz. The Panametrics V101 and V103 have nearly flat responses from 100 kHz to 1 MHz. The Valpey-Fisher Pinducer is 10–30 dB less sensitive compared to the other four sensors from 50 to 600 kHz. Table 3 lists the peak sensitivity (and its corresponding frequency) and maximum resolution (Sect. 4.2) of the five sensors.

In the 1–10 kHz frequency band, all five sensors have slopes close to 40 dB/decade indicating that they all are sensitive to acceleration in this band. The oscillations that are common for the $I(\omega)$ of all the sensors is due to a slight mismatch of the resonant/anti-resonant peaks between $U(\boldsymbol{x}, \omega)$ and $S(\boldsymbol{x}, \omega)$, evident in Fig. 5e.

3.4 Aperture Effect

For waves propagating in a given test specimen, at high frequencies when the wavelength is less than sensor's aperture, multiple wavelengths will average out in the sensor's area of contact, causing decreased amplitude in the recorded signal. Such an effect is called the aperture effect (e.g. [7,22,33,34]). For epicenter calibration described above, (position 1 in Fig. 2), the incidence angle = 90° so all wave motion is in phase across the face of the sensor, and the aperture effect is minimized. However, in some circumstances a surface calibration is preferred. In this case, incidence angle = 0° and aperture effect will affect sensitivity at high frequencies.

3.4.1 Theory

Past efforts have modeled the aperture effect while assuming a straight-line wavefront incident on a circular sensor (e.g. [22]), described by the source-sensor geometry of position 2 in Fig. 2 (incidence angle = 0°). Displacement is then

$$u(\boldsymbol{x}, t) = B \cos(kx - \omega t), \tag{9}$$

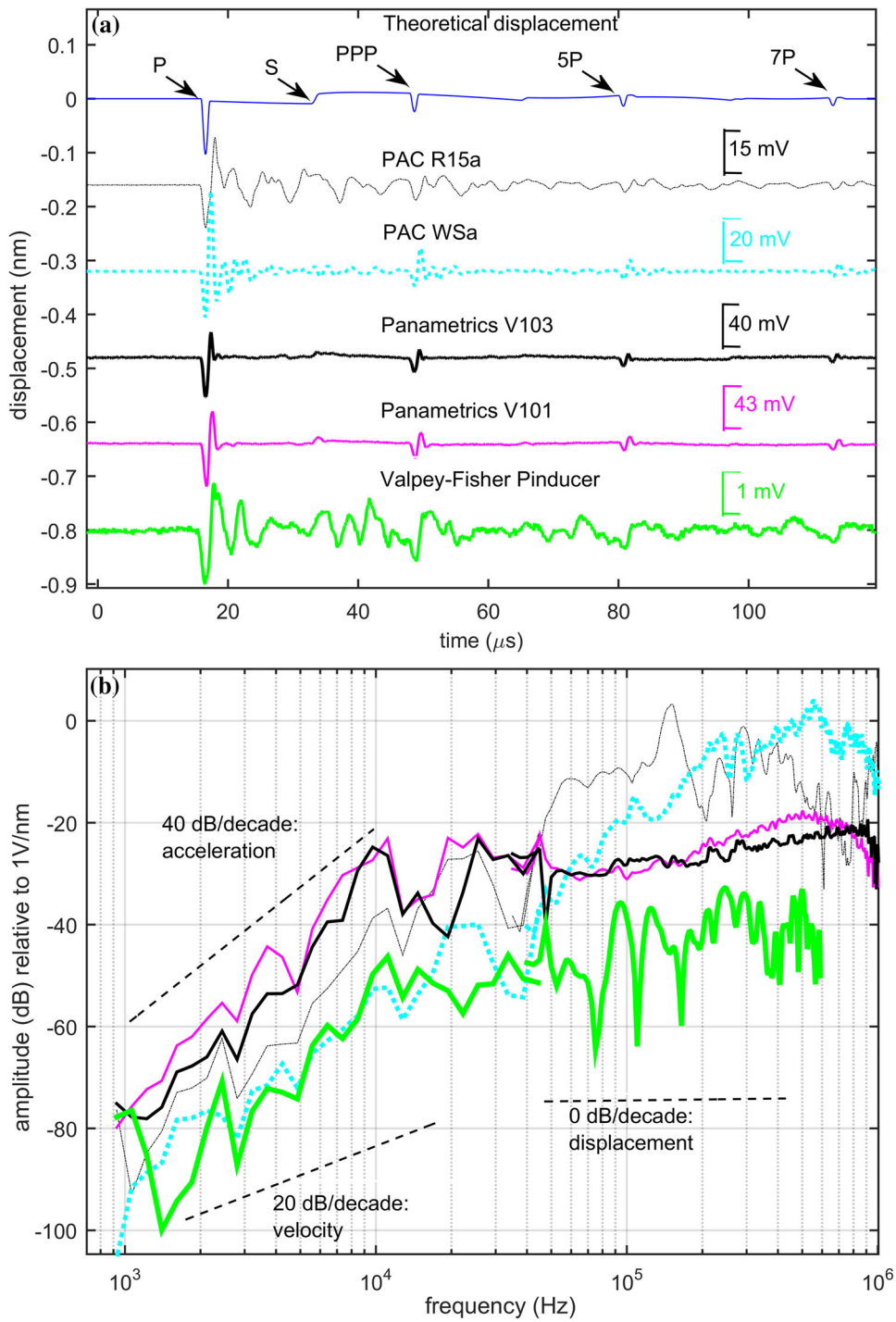

Fig. 7 Calibration results for five commercial sensors. **a** Top trace is the theoretical displacement for a 0.5 mm ruby ball source at the epicenter location, followed by the recorded signal of the five commercial sensors, as labeled. **b** Concatenated $I(\omega)$ computed using FE analysis for low frequencies and generalized ray theory for high frequencies. Different reference lines indicate displacement, velocity, and acceleration

where k is the scalar wavenumber and ω is the angular frequency.

The sensor response is defined as the surface integral of the displacement over the sensor's face combined with its local sensitivity, which is often assumed to be uniform across the sensor face (e.g. [7]) but is sometimes treated as nonuniform (e.g. [34]). The aperture function is the ratio between the surface integral and the initial wave equation. When uniform sensitivity across the sensor face is assumed, it and takes the form of a Bessel function of the first kind [22]:

$$\text{Aperture function} = \frac{4J_1(k\phi/2)}{k\phi}, \tag{10}$$

where ϕ is the sensor aperture, or diameter.

The wavenumber k can be expressed as $2\pi f/C$ (where C is wave speed in the medium). For surface calibrations,

Table 3 Peak sensitivity and max resolution for commercial sensors coupled to aluminum with hot glue

Sensor	Peak sensitivity (V/nm)	Frequency (kHz)	Max. resolution (pm)
PAC R15a	1.1	150	2
PAC WSa	1.2	560	1
Panametrics V101	0.10	500	10
Panametrics V103	0.079	910	12
Valpey-Fisher Pinducer	0.012	250	60

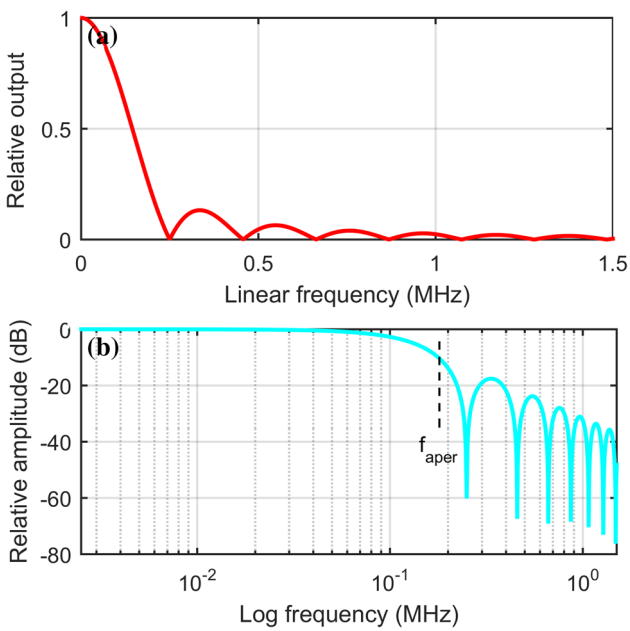

Fig. 8 Aperture function of the V103 sensor at the Rayleigh wave speed at 0 incidence angle. **a** Linear frequency, as seen in [22]. **b** The same plot is converted to logarithmic frequency and amplitude to highlight the lobes at higher frequencies

most of the wave energy that reaches the sensor is traveling at the Rayleigh wave speed C_R, so we use C_R to compute $f_{\text{aper}} = \frac{C_R}{\phi} = 200$ kHz. Figure 8 shows the theoretical aperture function of the V103 sensor ($\phi = 12.7$ mm) against frequency in both linear and log scale. Sensor output is unaffected by the aperture for frequencies lower than f_{aper}.

3.4.2 Demonstrating the Aperture Effect

Figure 9 demonstrates the aperture effect by comparing the epicenter (position 1) and surface (position 2) calibration curves for the Panametrics V101 ($\phi = 25.4$ mm, $f_{\text{aper}} = 102$ kHz), V103 ($\phi = 12.7$ mm, $f_{\text{aper}} = 200$ kHz), and Pinducer ($\phi = 2.6$ mm, $f_{\text{aper}} = 1$ MHz). $I(\omega)$ at positions 1 and 2 match to within 10 dB for frequencies less than f_{aper}. At frequencies higher than f_{aper}, the aperture effect causes the calibration curve to decrease in the form of a series of lobes, in agreement with the theoretical aperture function shown in Fig. 8. Each epicenter $I(\omega)$, scaled by its corresponding theoretical aperture function determined from Eq. 10, is also shown in Fig. 9 to illustrate the moderate agreement. The aperture effect is minimal in the Pinducer due to its small sensor diameter.

Besides utilizing Eq. 10, other ways to account for the aperture effect discretize the sensor surface into regions whose dimensions are determined by the minimum wavelength of interest ($\lambda_m = C_R/f_0$ where C_R is the Rayleigh surface wave speed). A forward approach assigns a weighting function to the Green's function in each discretized region based on its area and local sensitivity. They are then superposed into a finite receiver Green's function [33]. Another approach is to solve for the weighting function as an inverse problem, using iterative deconvolution techniques [35].

4 Discussion

4.1 Comparison with Previous Studies

The general shape of $I(\omega)$ and the location of resonances for the different sensors obtained in this study and shown in Fig. 7 matches well with results reported by Ono [6] using face-to-face reciprocity calibration. For example, for the PAC R15a, both studies identify the peak sensitivity at about 150 kHz with a secondary resonance peak at about 300 kHz that is 6 dB lower in amplitude. Both studies indicate that the V101 is about 5 dB more sensitive than the V103 in the 300–600 kHz band and both studies identify the broad resonant peaks of the V101 and V103 close to the published values of 500 kHz and 1000 kHz, respectively.

The absolute sensitivity of AE and ultrasonic sensors is more difficult to measure accurately, since recorded signal amplitudes are affected by the type of couplant used and the impedance contrast between sensor and test material. The absolute amplitude of the ball impact source function depends on the change in momentum of the ball, so the measured coefficient of restitution must be used to make a small (2.6 dB) correction to Hertz theory, as described in Sect. 2.3. In general, the sensitivities reported in Table 3 are lower than those reported by Ono [6]. The main cause for the discrepancy is coupling type (hot glue vs. Vaseline), as described in the next section. Other sources of error may be differences in the impedance of the test specimen material (aluminum versus face-to-face sensor calibration), differing sensor response between different sensors of the same model, or inaccuracy of the Hertz contact model, particularly for the tiny ruby ball and frequencies close to 1 MHz.

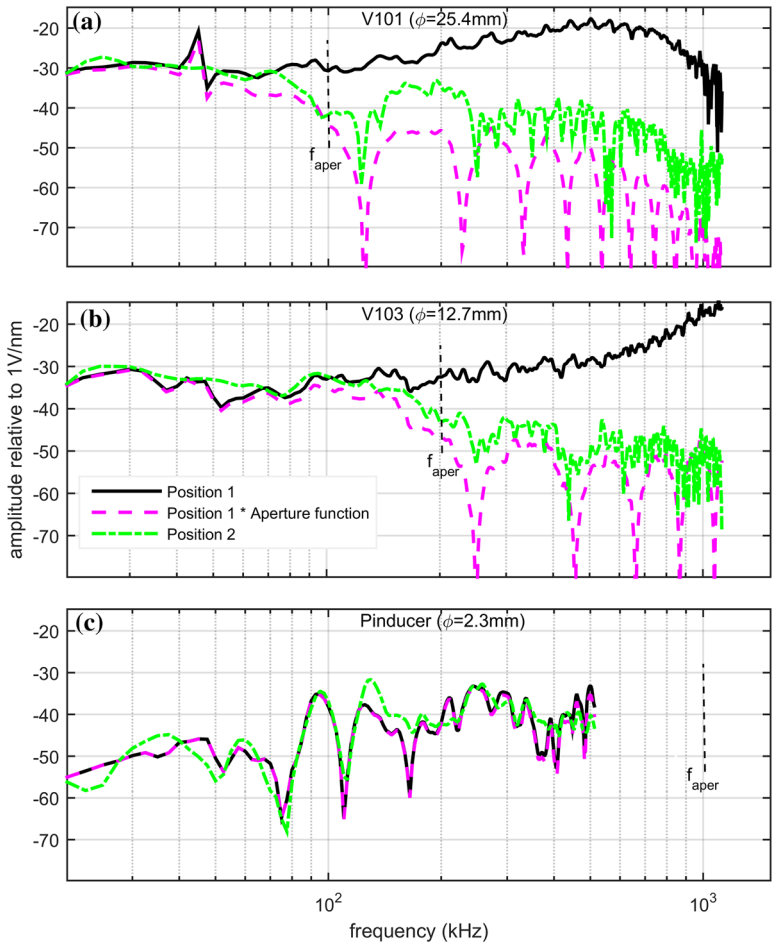

Fig. 9 Aperture effects on V101, V103, and Pinducer. In each subplot the black trace is $I(\omega)$ estimated from a recorded signal and mechanical disturbance at the epicenter location, the green curve is $I(\omega)$ from position 2, and the red curve is the black curve scaled by the sensor's theoretical aperture function determined from Eq. 10. The calibration curves are plotted up to when the SNR drops to 10 dB. The source used for the V101 and V103 sensors is the 0.5 mm ruby ball. The source used for the Pinducer is the 0.8 mm Titanium ball. In **c** the solid and dashed red curves overlap since f_{aper} of the Pinducer is over 1 MHz (Color figure online)

4.1.1 The Effects of Hot Glue as a Couplant

The calibration results reported in Fig. 7 correspond to the sensitivity of the various sensors when coupled to aluminum using hot glue. To better compare our results to those of Ono [6], we conducted an experiment to examine the frequency-dependent attenuation by hot glue compared to Vaseline which was used in those experiments. Two identical V103 sensors (sn 952678 and sn 1116882) were placed on the bottom surface of the test plate at locations symmetric about the epicenter (position 3 in Fig. 2). One was coupled with a 0.82 mm thick layer of hot melt glue as in all previous experiments and the other was coupled with Vaseline and taped to the specimen using a 0.5 m-long section of packaging tape. The plate was then excited by the impact of a 0.8 mm Titanium ball, and the fracture of a 0.2 mm diameter thin wall glass capillary tube [16]. In this experiment the source characteristics, wave propagation, digitizer, and cable length are carefully kept constant, leaving the coupling method as the only variable. The sensors were then switched and experiments repeated in order to account for any differences between the two individual V103 sensors (found to be $\leq$ 6 dB). Figure 10a compares the two coupling methods for the 0.8 mm titanium ball dropped from a height of 110 mm onto a 51 mm thick aluminum plate. Figure 10b shows the average of spectral ratios of the two coupling methods obtained from all combinations of sources and sensor positions. Differences between the two coupling methods are modest ($<$ 6 dB) below 6 kHz, but for higher frequencies, attenuation of hot glue compared to Vaseline increases at roughly 8 dB/decade from 6 to 600 kHz, with notable deviations from this overall trend. This comparison demonstrates the important effect of sensor coupling on both the amplitude and the shape of recorded signals.

4.2 Frequency Dependent Resolution

The smallest amplitude wave that an AE and ultrasonic sensor can detect ($R(\omega)$) is obtained from

$$R(\omega) = \frac{S_{\text{nf}}(\omega)}{I(\omega)}, \tag{11}$$

where $S_{\text{nf}}(\omega)$ is the spectrum of the noise floor obtained from the Fourier transform of a recorded signal before the first wave arrival (all noise signal). Better resolution is achieved

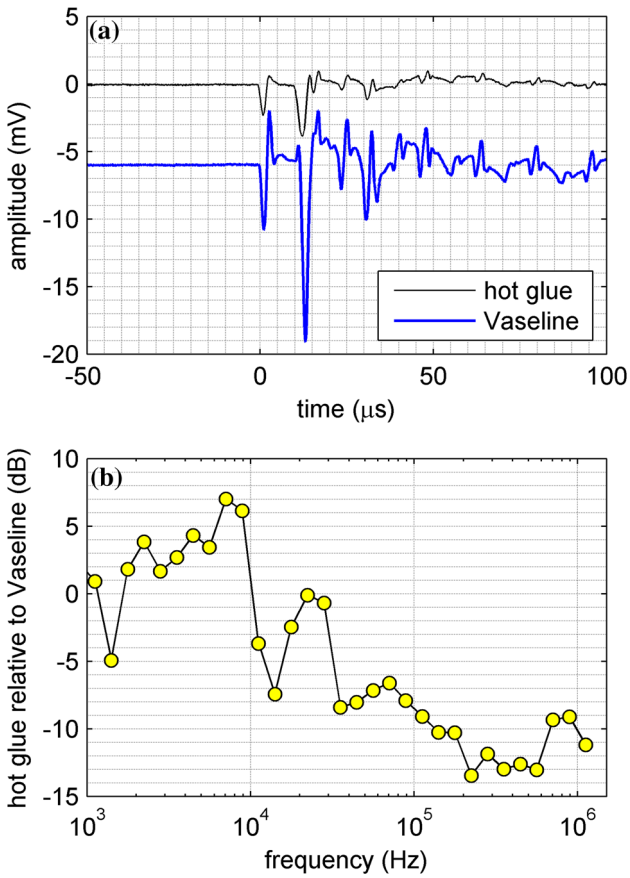

Fig. 10 Comparison between hot glue and Vaseline showing how hot glue attenuates and affects the frequency content of recorded signals (relative to Vaseline). **a** Signals were recorded while two V103 sensors were placed in locations symmetric about the source impact location (position 3 in Fig. 2). All differences between the signals should be due to coupling. **b** The average of spectral ratios of the two couplingmethods obtained from different source types and by switching the location and coupling type of the two sensors (see text)

with a lower noise floor, so it is important to reduce noise in all components of the recording system (preamps, cables, etc.). Figure 11 shows the sensor resolution (or rather, instrument resolution for an in-situ calibration) as a function of frequency from 60 kHz to 1 MHz obtained with our Elsys TraNet EPCe data recorder while a 200 mV digitization range is selected on the recording system. Spectral averaging (described in Appendix A) is applied. It is possible that the limiting noise floor was not in the sensors themselves but due to other links in our recording system (cable, digitizer, couplant), so these resolution estimates should be considered as upper bounds.

The peak resolution (in pm) of each sensor is listed in Table 3. The PAC sensors (WSa, R15a) can resolve displacements down to 1 pm from 100 kHz to 1 MHz. The Panametrics sensors (V101, V103) are sensitive down to 10 pm from 100 kHz to 1 MHz. The pinducer has the lowest resolution, only capable of detecting down to ∼100 pm. Since

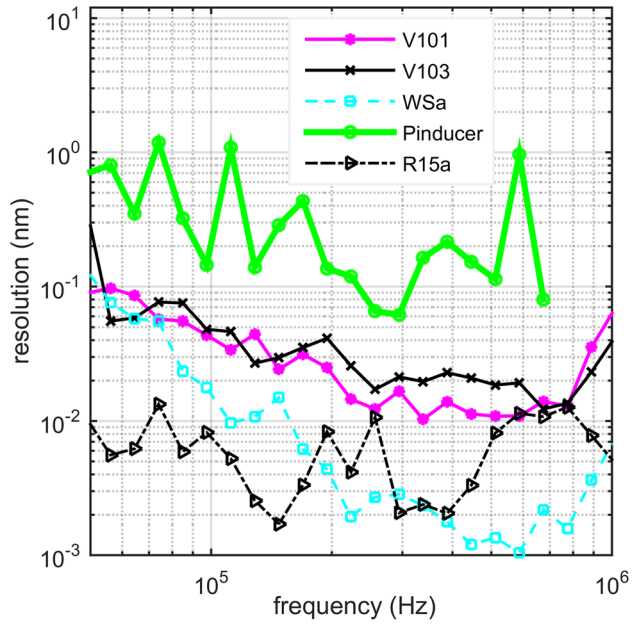

Fig. 11 Frequency dependent resolution for five commercial sensors when coupled to aluminum using hot glue. The best resolution (lowest value) for each sensor is achieved near its specified resonant frequency

hot glue was shown to attenuate signal by 8–15 dB in this frequency band (when compared to Vaseline), better resolution could be achieved with a different choice of couplant.

4.3 Displacement, Velocity, or Acceleration?

In this study all sensors are calibrated against the theoretical displacement (Eq. 3), therefore $I(\omega)$ is an estimate of the displacement instrument response spectrum. A flat $I(\omega)$ indicates an ideal displacement sensor. Taking a derivative in the time domain is equivalent to multiplying by $i\omega$ in the frequency domain [19]. Therefore, velocity has a slope of 20 dB per decade frequency while acceleration has a slope of 40 dB per decade frequency. In the time domain, the shape of the longitudinal wave arrivals (P, PPP, 5P, etc.) would be perfect double-sided pulses for a velocity sensor and a single-sided pulse for a displacement sensor. The V101 instrument response has a slope near 20 dB per decade in the ∼70 kHz to 500 kHz frequency band (Fig. 7b) and shows double-sided pulses in time domain (Fig. 7a) and therefore acts as a velocity sensor in that frequency band. The V103 response has a slope between 0 and 20 dB in the 50 kHz to 1 MHz frequency band and in the time domain the wave arrivals are double-sided pulses with the first side of the pulse stronger than the second side (Figs. 5a, 7), so the V103 about halfway between a displacement and a velocity sensor in this frequency band. The PAC R15a and Pinducer are strongly resonant and therefore cannot be categorized.

The PAC WSa has a slope of approximately 20 dB/decade from 100 kHz to 1 MHz. Figure 12 demonstrates the calibra-

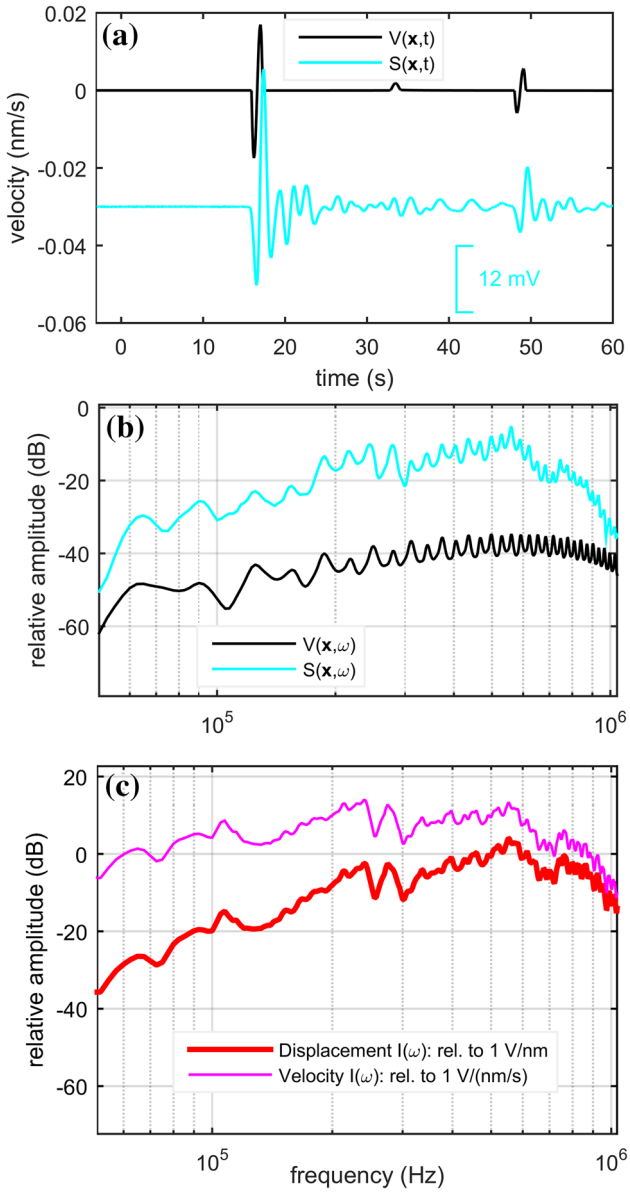

Fig. 12 Calibration of PAC WSa against velocity. **a** Comparison of theoretical velocity $v(\boldsymbol{x}, t)$ against the recorded signal $s(\boldsymbol{x}, t)$. **b** The Fourier transform of $v(\boldsymbol{x}, t)$ and $s(\boldsymbol{x}, t)$. **c** The velocity instrument response spectra and the displacement response spectra

tion of the PAC WSa against theoretical velocity ($v(\boldsymbol{x}, t)$). The theoretical velocity is computed by convolving the force–time function of the source with the time derivative of the Green's function for the epicenter location:

$$v(\boldsymbol{x}, t) = f(\boldsymbol{\xi}, \tau) * \frac{d}{dt} G_{33}(\boldsymbol{x}, t; \boldsymbol{\xi}, \tau), \tag{12}$$

The velocity instrument response is then computed in a fashion similar to Eq. 3:

$$I(\omega) = \frac{S(\boldsymbol{x}, \omega)}{V(\boldsymbol{x}, \omega)}, \tag{13}$$

where $V(\boldsymbol{x}, \omega)$ is the FT of the theoretical velocity, $v(\boldsymbol{x}, t)$. Note that the velocity instrument response is equivalent to multiplying the displacement instrument response by $i\omega$ in the frequency domain. This additional calibration process shows that the PAC WSa is most sensitive to velocity at ~230 kHz.

5 Conclusion

This paper demonstrates a technique to calibrate AE and ultrasonic sensors using a ball impact as a calibration source and a thick aluminum plate as a test block. Following previous work [16], recorded signals were compared to the mechanical disturbance (surface displacement time history) felt by the sensor, which is calculated from theory. Generalized ray theory and the FE method were combined to achieve a broadband calibration effective from 1 kHz to 1 MHz, spanning three decades of frequency. The 3D FE model was verified at high frequencies against the generalized ray theory and was verified at low frequencies by a PCB accelerometer. This serves as an inexpensive substitute for a high-fidelity reference sensor or laser vibrometer.

We are interested in how the sensors behave in practice, and the calculated instrument response $I(\omega)$ includes the effects of coupling and other characteristics of the recording system. We found that attenuation caused by the couplant (hot glue in the current study) is not negligible at higher frequencies (> 10 kHz). Most of the calibrations reported here were performed in the epicenter position, where the sensor under test is located on the opposite side of the plate and directly beneath the location of ball impact. For surface calibrations, the aperture effect can no longer be ignored and we demonstrated how this affects sensor response at high frequencies.

The broadband calibration techniques proposed in this paper allow us to better understand the relative merits of different AE and ultrasonic sensors. In addition to having a resonant frequency, a sensor measures different physical quantities at different frequency bands with varying sensitivity. All of the sensors studied here act nearly as accelerometers in the 1–10 kHz band and are closer to velocity or displacement sensors in the 100 kHz to 1 MHz band. Quantification these frequency-dependent attributes enables quantitative analysis of source parameters including the magnitude, radiated energy, and source dimensions in space and time. This study focused on the amplitude of the instrument response—since that is all that is needed to determine the above source parameters—and ignored phase, which is needed to simulate the sensor's effects in the time domain. Future work will be focused on applying the technique to sensors coupled to other materials such as rock, plastic, and concrete. These materials will require a consideration of viscoelasticity, intrinsic attenuation, and scattering.

Acknowledgements Data were acquired from experiments conducted at Cornell University. The authors would like to acknowledge W. Sachse for lending us some of the sensor models, S. Schnabel for reading over the manuscript, and R. Bhaskaran and D. Kammer for help with finite element modeling.

Compliance with ethical standard

Conflict of interest The authors declare that they have no conflict of interest.

Appendix A

Boundary conditions certainly affect displacement output measured in the center of the plate, yet high-frequency waves, due to their short wavelength, will be minimally affected by the boundary conditions, at least for short time durations after the time of impact. This appendix describes a physical experiment that probes the effects of the boundary conditions in the experiments. We explore the frequency below which boundary conditions start to affect the displacement-time history in order to guide how we construct the boundary conditions for the FE model.

Figure 13b shows two kinds of boundary conditions selected for comparison: the aluminum plate sitting flat and vertical on two pieces of 90 × 90 mm wooden blocks topped with a 1.6 mm thick layer of cork. When the plate was vertical, we introduced impact onto the plate by attaching a piece of string to the ball and swinging it in a pendulum-like manner so that the ball hit the center of the plate from the surface-normal direction (illustrated in Fig. 13b). To keep the boundary condition as the sole variable, for each source we only compared ball drop/swing trials of equal amplitude. The spectra of recorded ground motions from different boundary conditions were consistent within 6 dB up to their respective corner frequencies and down to 5 kHz before the SNR dropped to 1. The comparison was further extended to lower frequencies by using a hammer tap as the source. The spectral estimates of the hammer tap were resampled into 17 equally-spaced intervals per decade frequency (as described in Sect. 2.1). As shown in Fig. 13a, down to approximately 50 Hz (SNR drops to 1), the spectra from two boundary conditions were consistent to within 6 dB. Therefore, this physical experiment shows that the recorded signal at the epicenter location is relatively indifferent to the boundary conditions at least for the first 50 ms and down to about 50 Hz.

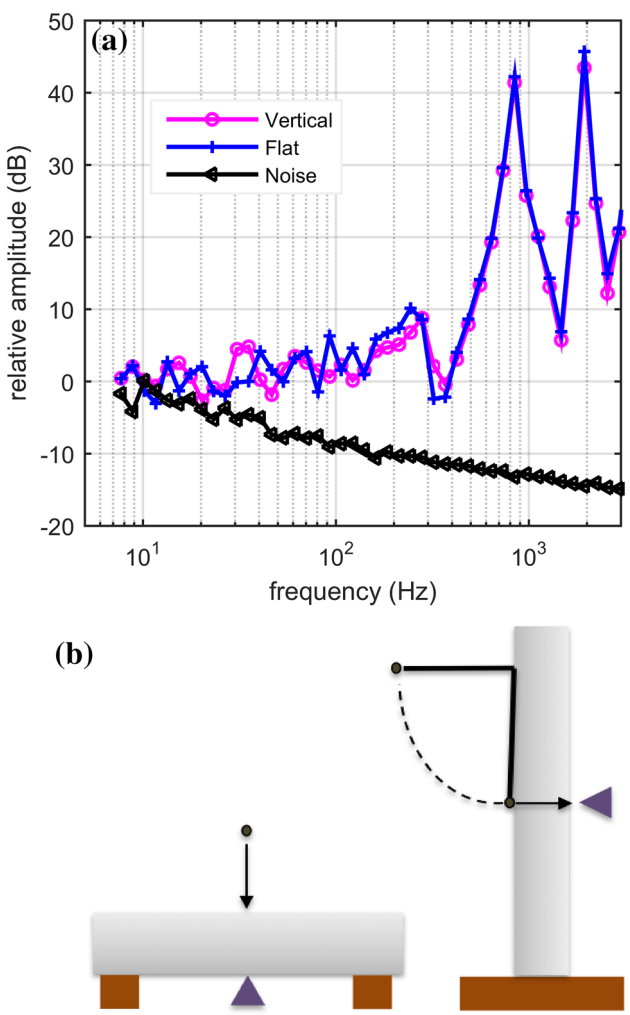

Fig. 13 Boundary condition comparison. **a** Comparison of the Fourier transform of signals recorded with different boundary conditions using a hammer tap source and keeping source-sensor geometry constant. **b** Setups for the flat/vertical boundary conditions. The black arrows indicate the direction of impact and the purple triangle represents the sensor under testing

References

1. Li, B.Q., Einstein, H.H.: Comparison of visual and acoustic emission observations in a four point bending experiment on Barre Granite. Rock Mech. Rock Eng. **50**(9), 2277–2296 (2017)
2. McLaskey, G., Lockner, D., Kilgore, B., Beeler, N.: A robust calibration technique for acoustic emission systems based on momentum transfer from a ball drop. Bull. Seismol. Soc. Am. **105**(1), 257–271 (2015)
3. Goodfellow, S., Young, R.: A laboratory acoustic emission experiment under in situ conditions. Geophys. Res. Lett. **41**(10), 3422–3430 (2014)
4. Taylor, S., Brodsky, E.: Granular temperature measured experimentally in a shear flow by acoustic energy. Phys. Rev. E **96**(3), 032913 (2017)
5. Hatano, H., Watanabe, T.: Reciprocity calibration of acoustic emission transducers in Rayleigh-wave and longitudinal-wave sound fields. J. Acoust. Soc. Am. **101**, 1450–1455 (1997)
6. Ono, K.: Calibration methods of acoustic emission sensors. Materials **9**(7), 508 (2016)
7. Goujon, L., Baboux, J.C.: Behaviour of acoustic emission sensors using broadband calibration techniques. Meas. Sci. Technol. **14**, 903–908 (2003)

8. Ono, K., Cho, H., Matsuo, T.: Transfer functions of acoustic emission sensors. J. Acoust. Emiss. **26**, 72–90 (2008)
9. ASTM Standard E1106-86: Standard method for primary calibration of acoustic emission sensors. ASTM International, West Conshohocken (2002)
10. Sansalone, M., Carino, N., Hsu, N.: A finite element study of transient wave propagation in plates. J. Res. Natl Bureau Stand. **92**(4), 267–278 (1987)
11. Sause, M., Hamstad, M., Horn, S.: Finite element modeling of conical acoustic emission sensors and corresponding experiments. Sensors Actuators A **184**, 64–71 (2002)
12. McLaskey, G., Glaser, S.: High-fidelity conical piezoelectric transducers and finite element models utilized to quantify elastic waves generated from ball collisions. In: SPIE Smart Structures and Materials + Nondestructive Evaluation and Health Monitoring, pp. 72920S-72920S. International Society for Optics and Photonics, Bellingham (2009)
13. Breckenridge, F., Proctor, T., Hsu, N., Eitzen, D.: Some notions concerning the behavior of transducers. In: Proceedings of the Eighth International Acoustic Emission Symposium. Progress in Acoustic Emission III. The Japanese Society of NDI, Tokyo, Japan, pp. 675–684 (1986)
14. Hsu, N., Simmons, J., Hardy, S.: Approach to acoustic emission signal analysis—theory and experiment. Mater. Eval. **35**, 100–106 (1978)
15. Manthei, G.: Characterisation of acoustic emission sensors. In: 29th European Conference on Acoustic Emission Testing, Vienna, Austria (2010)
16. McLaskey, G., Glaser, S.: Acoustic emission sensor calibration for absolute source measurements. J. Nondest. Eval. **31**, 157–168 (2012)
17. Lobkis, O., Weaver, R.: On the emergence of the Green's function in the correlations of a diffuse field. J. Acoust. Soc. Am. **110**(6), 3011–3017 (2001)
18. Shapiro, N., Campillo, M.: Emergence of broadband Rayleigh waves from correlations of the ambient seismic noise. Geophys. Res. Lett. **31**(7), L07614 (2004)
19. Bracewell, R.: The Fourier Transforms and Its Applications. McGraw-Hill, Boston (2000)
20. Sachse, W., Ceranoglu, A.: Experiments with a well-characterized acoustic emission system. In: Proceedings of Ultrasonics International Congress, vol. 79(1), pp. 138–145 (1979)
21. Hsu, N., Breckenridge, F.: Characterization of acoustic emission sensors. Mater. Eval. **39**, 60–68 (1981)
22. Eitzen, D., Breckenridge, F.: Acoustic emission sensors and their calibration. In: Miller, R., McIntire, P. (eds.) Nondestructive Testing Handbook Second Edition, vol. 5: Acoustic Emission Testing, pp. 121–132. American Society for Nondestructive Testing, Columbus (1987)
23. Pao, Y., Gajewski, R., Ceranoglu, A.: Acoustic emission and transient waves in an elastic plate. J. Acoust. Soc. Am. **65**(1), 96–105 (1979)
24. Hsu, N.: Dynamic Green's functions of an infinite plate—a computer program. Technical Report No. NBSIR 85-3234. National Bureau of Standards, Center for Manufacturing Engineering, Gaithersburg (1985)
25. Hsu, N.: Acoustic emission simulator. U.S. Patent 4,018,084 (1977)
26. Ono, K., Cho. H.: Proceedings of 28th European Conference on Acoustic Emission Testing, Krakow, pp. 25–30 (2008)
27. Scruby, C., Drain, L.: Laser Ultrasonics Techniques and Applications. CRC Press, Boca Raton (1990)
28. McLaskey, G., Glaser, S.: Hertzian impact: experimental study of the force pulse and resulting stress waves. J. Acoust. Soc. Am. **128**, 1087–1096 (2010)
29. Goldsmith, W.: Impact. Dover Publications, New York (2001)
30. Johnson, L.: Green's function for Lamb's problem. Geophys. J. Int. **37**(1), 99–131 (1974)
31. Prosser, W., Hamstad, M., Gary, J., O'gallagher, A.: Finite element and plate theory modeling of acoustic emission waveforms. J. Nondestruct. Eval. **18**(3), 83–90 (1999)
32. Sansalone, M., Street, W.: Impact Echo: Nondestructive Evaluation of Concrete and Masonry. Bulbrier Press, Ithaca (1997)
33. Lalos, J., Pozar, T., Mozina, J.: High-frequency calibration of piezoelectric displacement sensors using elastic waves induced by light pressure. J. Mech. Eng. **61**, 533–542 (2015)
34. Dia, S., Monnier, T., Godin, N., Zhang, F.: Primary calibration of acoustic emission sensors by the method of reciprocity. Theoretical and experimental considerations. In: 30th European Conference on Acoustic Emission Testing & 7th International Conference on Acoustic Emission. University of Granada, 12–15 September (2012)
35. Chang, C., Sachse, W.: Separation of spatial and temporal effects in an ultrasonic transducer. In: Review of Progress in Quantitative Nondestructive Evaluation, pp. 139–143. Springer, New York (1986)